Unravelling Charge-transfer in Pd to pyrrolic-N bond for superior electrocatalytic performance

Lipipuspa Sahoo,[1] Sanjit Mondal,[1] A. Gloskovskii ,[2] Arunabhiram Chutia,[3,*] Ujjal K. Gautam[1,*]

[1]Department of Chemical Sciences, Indian Institute of Science Education and Research (IISER)-Mohali, Sector 81, Mohali, SAS Nagar, Punjab 140306, India

[2]DESY Photon Science, Deutsches Elektronen-Synchrotron, 22603 Hamburg, Germany

[3]School of Chemistry, University of Lincoln, Lincoln LN6 7TS, United Kingdom

* ujjalgautam@gmail.com, ujjalgautam@iisermohali.ac.in, achutia@lincoln.ac.uk, achutia@gmail.com

Abstract

Fuel-cells require large quantities of Pt for oxygen reduction reaction (ORR) to subvert the activity-loss during prolonged use. Pd can complement Pt in the near future by exhibiting a similar activity and stability in alkaline fuel-cells. Herein we show that by depositing Pd atom-by-atom on an N-doped reduced graphene oxide (NRGO), it is possible to create a strong bond between Pd and pyrrolic-fraction of the N-moieties. This bond further strengthens in the presence of an oxygen containing functional-group accompanied by a profound charge-transfer from the Pd 3*d*-orbitals to the 2*p*-orbitals of C, N and O, thereby lowering the Pd-3*d* binding-energy and the resulting Pd/NRGO exhibits a very high ORR activity ($E_{1/2}$ = 0.93 V *vs.* RHE) and stability ($\Delta E_{1/2}$ = 0.013 V after 15000 cycles). Usually pyridinic-N is considered for imparting high-performance while N-doping creates nearly as many pyrrolic-N in graphene-substrates, the role of which is evidenced in this study.

Introduction

Palladium as an electrocatalyst is getting increasing attention for oxygen reduction reaction (ORR) in alkaline fuel cells (AFCs) due to their higher abundance, lower cost and a potential to replace the commercially used Pt.[1–4] Recent investigations have shown that the electrocatalytic efficiency of the Pd-based catalysts can be improved systematically and significantly to match those of Pt by adopting innovative design strategies, tailoring their surfaces by means of facet engineering or alloy formation and tuning of substrate-catalyst interactions.[5–11] However, two outstanding challenges in AFCs while using Pd nanocrystals (NCs) remain to-date: i) overcoming the sluggish ORR kinetics to further reduce the Pd requirement to match a target set by U.S. Department of Energy, and ii) the absence of sustained high-catalytic activity for prolonged time-periods under the electrochemical operating environments.[6,8,12] Therefore in the existing device prototypes, a larger amount of noble metal is loaded on to the electrode surfaces to attain a sufficient durability.[2]

Forming alloy nanocrystals of Pd with other metals such as Co, Ni, Cu etc. has emerged as a preferred strategy to modulate the surface electronic structure for improved catalytic activity, and to reduce the noble metal load at the same time.[7–9,11–15] The electrons in the 'other' metals hybridize with the *d* electrons of Pd to lower the '*d*-band center' effecting a favorable modulation of the bond-strengths of the ORR intermediates.[16,1718] Besides, the lattice strain invoked by smaller sizes of the alloying atoms also helps in attenuating the intermediate binding energies.[7,8,19,20] Very recently, Bi was shown to form alloy NCs with Pd, exhibiting a very high ORR $E_{1/2}$ = 0.92 V *vs.* RHE due to the weakening of the surface Pd-O bonds.[9] However, the activity loss was >40% after 10000 cycles. Overall, the large body of work done to date suggests that a high mass-activity in alloys is accompanied by a rapid loss of performance.[1,9,21] Another general disadvantage in using alloys may arise due to a continuous change of their compositions during catalysis due to the high chemical reactivity of the non-noble components.[11] On the other hand, extremely high stability up to 100000 cycles was achieved recently by using alloy thin-films, but even the initial activities were poorer than the deactivated performances of the nanoparticulate catalysts due to a larger catalyst load. [13]

Alternatively, it has long been predicted that metal to substrate charge-transfer interactions (MSI) can be used for regulating the metal-oxygen bond-strengths[22–24] and was demonstrated experimentally using various substrates such as sp^2 carbon derivatives recently for improved ORR activity.[25,26] The benefits of using graphene as a substrate include two additional aspects i.e. the defects provide anchoring points to the metal to offer higher stability and prohibits the Ostwald ripening of the nanoparticles during growth to improve catalyst surface-area. First-principle studies have revealed that the binding of Pd on a graphene vacancy improves due to the hybridization of the *d, s* and *p* states of the Pd with the defect sp^2 orbitals,

shifting the *d*-band away from the Fermi energy.[23] The binding becomes even stronger when using N-doped graphene due to higher electronegativity of N.[24] Several primary N sites can be defined in a graphene network: graphitic N (N atoms substituting C atoms, N_G), pyridinic N (double coordinated N atom in a hexagon ring, N_{pyd}), pyrrolic N (N atoms in a five-membered ring, N_{Pyr}), each of which influences the metal-support interactions differently.[27,28] The role of N_{pyd} and N_G in ORR has been intensely scrutinized.[24,27,28] The hybridization of the sp^2 dangling bonds and the metal *d* orbitals leads to a pronounced charge-transfer and a Pd-N_{pyd} bond that can, at times, be so strong that even a reducing atmosphere which removes oxygen from the Pd surface cannot reduce the Pd-N bonds. As a result the metal surface retains $M^{\delta+}$ charge to attenuate the catalytic properties.[29] N_G enhances metal adsorption by activating the C atoms next to it.[24] On the other hand, N doping of carbon can lead to high N_{Pyr} contents also, varying in the range of 15-80% under different processing conditions.[30] However the participation of N_{Pyr} in ORR has not been experimentally established so far, even though its effect on the growth of Pd nanoparticles was observed.[31] A couple of studies also indicated that Npyr may influence electrocatalytic activities in other applied potential ranges, though it is not clear if such effects arise from Npyr alone or due to other changes in the electrocatalysts.[32,33] Moreover, little attention has been given towards elucidating the nature of metal-N_{Pyr} interactions and therefore the role of N_{Pyr} in MSI remain a 'missing-link' in complete understanding of the role of N in ORR.

Finally, the π* electrons in N-doped graphene exhibits a "donor-like" behavior.[24] This gave us a notion that the concentration of Pd^{2+} ions in a solution containing N-doped reduced graphene oxide (NRGO) will increase near the N-centers. Thus when these cations are reduced to Pd(0) *in-situ*, the deposition of the NCs will primarily take place at the N centers and these should offer a better ORR performance and stability when compared with a mixture of pre-formed Pd NCs with NRGO. Such a strategy was recently adopted to deposit Pd on N-doped carbon by thermally decomposing a novel 1-nepthylamine-Pd precursor. However the $E_{1/2}$ was only 0.76 V *vs*. RHE, probably due to a carbon coating developed over the Pd nanocrystals. [26]

Motivated by a strong possibility to improve the ORR activity and stability, we have investigated the effect of simultaneous use of NRGO substrate and *in-situ* deposition of Pd NCs on the electrocatalytic properties in alkaline medium. The NRGO supported Pd NCs were significantly more active for ORR ($E_{1/2}$ = 0.93 *vs.* RHE and a mass-activity of 0.59 A/mg at 0.9 V *vs.* RHE) as compared to the RGO supported ones. It also exhibited a very high stability with $\Delta E_{1/2}$ of only 0.13 meV after 15000 catalytic cycles. Furthermore, we found that the *in-situ* deposition is far more efficient than an *ex-situ* generated composite of pre-formed Pd NCs with NRGO. The enhanced performance was attributed to a strong Pd-N_{Pyr} binding and a pronounced N_{Pyr} to Pd charge-transfer. Density functional theory (DFT) studies have revealed that

the N_{Pyr} induces a strong Pd-NRGO MSI effect, accompanied by a loss of planarity of the graphene sheet, wherein the Pd atom stabilizes at the bridging sites of N_{Pyr} and its neighboring C atom. The proximity of an oxygen-containing functional group can further improve Pd-N_{Pyr} charge-transfer due to the hybridization of the O-*p* orbitals. Thus, from clear experimental evidences and theoretical understanding, this work demonstrates the necessity to develop strong N-Pd interactions by the simultaneous tailoring of both N_{Pyr} and N_{Pyd} interactions for improved performance and durability in fuel cells.

Experimental section

Chemicals and Materials: Palladium chloride ($PdCl_2$, <99%, Alfa Aesar), Polyvinylpyrrolidone (PVP, MW~40000, Sigma Aldrich), Graphite powder (Alfa Aesar), $KMnO_4$ (Rankem), H_2SO_4 (Himedia), H_3PO_4 (Himedia), HCl (Himedia), H_2O_2 (Rankem), diethyl ether (Himedia), Melamine (Sigma Aldrich), KOH (Himedia), Methanol (Himedia). All the chemicals were used without further purification. All the experiments were performed in ultrapure water (resistivity of 18.2 MΩ).

Synthesis of Graphene oxide (GO): GO was prepared by a modified Hummers' method. In a typical synthesis, 133 ml of 9:1 mixture of conc. H_2SO_4/H_3PO_4 was slowly added to a beaker containing 1 g of graphite powder and 6g of $KMnO_4$ placed on an ice bath to maintain the solution temperature below 10 ºC. Afterward, the reactant mixture was heated at 55 ºC for 12 h with constant stirring. The green color solution was turned to dark brown after 12 h. Then the reaction mixture was cooled to room temperature, followed by the addition of ~130 g of ice and 1 ml of H_2O_2 (30%) which immediately changed the solution color to yellow indicating the formation of GO. The reaction mixture was washed in succession with 200 ml water, 200 ml HCl (30%), and 200 ml ethanol by repeated sonication and centrifugation. Finally, the product was precipitated in diethyl ether and dried in an oven at 60º overnight.

Synthesis of N-doped reduced graphene oxide (NRGO): 1.2 g of GO and 6 g of melamine were dispersed in 100 ml and 400 ml of water respectively under sonication. Melamine suspension was added into GO dispersion and kept under constant stirring for 12 h. Then the solution temperature was raised to 55 ºC in order to evaporate the water. The dried sample was ground using a mortar pastel and pyrolyzed inside a tube furnace under Ar atmosphere (with a heating rate of 5 ºC/min) at 350 ºC for 3 h subsequently at 850 ºC for 30 min. Finally, the furnace was naturally cooled to room temperature and NRGO samples were obtained.

Synthesis of reduced graphene oxide (RGO): 0.5 g of GO was pyrolyzed under Ar atmosphere inside a tube furnace at 350 ºC (with a heating rate of 5 ºC/min) for 3 h followed by 850 ºC for 30 min at a ramp rate of 5 ºC/min. The furnace was allowed to cool naturally.

Preparation of in-situ Pd/NRGO or Pd/RGO samples: In a typical synthesis, 0.5 g PVP (MW=40000) was dissolved in 8 ml water by magnetic stirring in a 50 ml beaker at 700 rpm until the solution becomes transparent. In order to prepare H_2PdCl_4, $PdCl_2$ (11.3 mg) was mixed with conc. HCl (11.6 M, 75 µL) by ultrasonication for 5 min and 2 ml of water was added. 15 mg of NGO was dispersed in 5 ml of water by ultrasonication. H_2PdCl_4 solution was added dropwise to the PVP solution under magnetic stirring at ~500 rpm and continued to stir for a few minutes to ensure homogeneity. The above reaction mixture was added to the NGO dispersion under vigorous magnetic stirring at ~700 rpm. After 20 minutes of stirring, the resulting solution was transferred into a 25 mL Teflon-lined stainless steel autoclave and kept at 200 °C in a preheated oven for 12 h. The oven was allowed to cool naturally. The obtained product was centrifuged at 13,500 rpm for 15 minutes to separate the Pd NPs loaded on NRGO and washed several times with water and ethanol to remove the excess PVP. Finally, the sample was dried overnight in an oven at 60 ºC and labeled as Pd/NRGO. Palladium loading on NRGO was varied from 15-50 % by varying $PdCl_2$ and PVP conc. in the reaction mixture. For comparison, Pd/RGO was prepared via the same procedure by replacing

NRGO with RGO. Bare Pd NPs were prepared by following via same procedure without addition of any carbon supprort. NRGO was treated in a similar reaction condition without any metal precursor and used for comparison.

Ex-situ synthesis of Pd/NRGO: As prepared Pd NPs (6.8 mg) were dispersed in 0.5 ml ethanol. 15 mg of NRGO was dispersed in 15 ml of water by ultrasonication for 10 min. Pd NP dispersion was added dropwise to the NRGO suspension. The reaction mixture was stirred for 12 h overnight. The sample was collected by centrifugation and washed several times water and ethanol and dried in an oven at 60 ^{o}C.

In all synthesis processes described above for the Pd containing samples, the solvent recovered after the synthesis and separation of the nanostructures appeared colorless suggesting that entire Pd salt was deposited on the graphene-based substrates. The same as further confirmed from the HAXPES studies.

Characterization: Transmission electron microscope (TEM) and high-resolution TEM (HRTEM) images were recorded with JEOL JEM-F200. Powder X-ray diffraction patterns were recorded using a Rigaku Ultima IV diffractometer with Cu Kα X-ray radiation (generator power setting: 40 mA and 40 kV) at a scanning rate of 1° min^{-1}. Raman spectra were recorded in a Renishaw Raman Spectrometer equipped with a 514 nm laser. Hard X-ray photoelectron spectroscopy (HAXPES) measurements were performed at P22 beamline at PETRA-III, DESY (Hamburg, Germany).[34] HAXPES experiments were carried out at a photon energy of 5946 eV.

Preparation of working electrode: 1.1 mg of Pd/NRGO *in-situ* was dispersed in 1 ml of nafion:isopropanol:water (in ratio of 0.5:1:4) solution by ultrasonication for 20 minutes. 4 µl of the above suspension was drop cast on to pre-cleaned glassy carbon (GC) rotating disk electrode (RDE) with a geometric surface area of 0.0707 cm^2 and dried overnight at ambient condition. The total loading of Pd was 1.41 µg or 20 µg/cm^2 on the electrode surface. Similarly, the metal loadings for Pd/NRGO *ex-situ*, Pd/RGO and Pt/C were maintained at 20 µg/cm^2 on the electrode surface.

Electrochemical measurements: The electrocatalytic performances were measured using a GC-RDE connected to CHI760E electrochemical workstation. A conventional three-electrode setup was used with Hg/HgO (0.1 M NaOH) as a reference electrode and Pt wire as a counter electrode. For comparison, all potential values were converted and plotted with respect to reversible hydrogen electrode (RHE). The cyclic voltammograms (CV) were recorded in Ar saturated 0.1 M KOH electrolyte with a sweep rate of 10 mV/s. The ORR polarization curves were recorded in O_2 saturated 0.1 M KOH with a sweep rate of 10 mV/s at a rotation rate of 1600 rpm. The kinetic current can be estimated from Koutecky–Levich (K-L) equation as follows:

$$1/I = 1/I_k + 1/I_d$$

Where, I, I_k, and I_d are experimentally measured current, kinetic current, and diffusion limited current respectively. The I_d term can be obtained from the Levich equation:

$$I_d = 0.62nFAD^{2/3}\upsilon^{-1/6}\omega^{1/2} C_{O2}$$

where n is the number of electrons involved in the reaction, F is Faraday's constant (96485 C/mol), A is the electrode area (0.0707 cm^2), D is the O_2 diffusion coefficient in 0.1 M KOH solution (1.9×10^{-5} cm^2 s^{-1}), υ is the kinematic viscosity of the electrolyte (1.01×10^{-2} cm^2 s^{-1}), ω is the angular frequency of rotation, $\omega = 2\pi f/60$, f is the rotation rate of RDE in rpm, and C_{O2} is the concentration of O_2 in 0.1 M KOH solution (1.21×10^{-6} mol cm^{-3}). The mass activity was calculated by estimating kinetic current and dividing it with Pd (or Pt) mass loading. The specific activity was determined by normalizing kinetic current with correspond electrochemically active surface area (ECSA). The ECSA was estimated using the following formula:

$$\text{ECSA} = \frac{Q_{Pd\ or\ Pt}}{\Gamma \times (mg\ Pd\ or\ Pt)}$$

where Q is the charge accumulated for reduction of $Pd(OH)_2$ or hydrogen adsorption region of Pt calculated from the CV. Γ is the charge deposited per unit surface area for the formation of $Pd(OH)_2$ (405 μC/cm^2) or monolayer adsorption of hydrogen on Pt surface (210 μC/cm^2).

The stability tests were performed at room temperature in the potential window of 0.6 to 1.1 V *vs.* RHE by applying cyclic sweeps in O_2 saturated 0.1 M KOH at 1600 rpm with a scan rate of 0.1 V/s up to 15000 cycles.

Methanol tolerance test: Methanol electro-oxidation was performed in 0.1 M KOH containing 0.1 M methanol using a scan rate of 50 mV/s in the potential range of 0.25 V to 1.45 V *vs.* RHE. ORR polarization curves were recorded in O_2 saturated 0.1 M KOH containing 0.1 M methanol with a scan rate of 10 mV/s in the potential range of 0.4 V to 1.15 V. Chronoamperometry measurements were performed at 0.6 V *vs.* RHE in the O_2 saturated 0.1 M KOH solution and methanol was added after 100 sec.

Computational details

Vienna Ab Initio Simulation Package (VASP) is used to perform spin polarized periodic density functional theory based quantum chemical calculations.[35] We employ the projector augmented wave (PAW) method and for the expansion of the plane-wave basis sets the cut-off energy is set to 550 eV, which gives bulk energies converged to within 10^{-5} eV.[36] We choose a convergence criterion of 0.01 eV Å^{-1} for the structural optimizations and a gamma centered k-point grid of 5×5×1 is employed. The revised Perdew-Burke-Ernzerhof (PBE) version of generalized gradient approximation (GGA), for solids, the PBEsol exchange and correlation functional is used to relax the structures and to perform the total energy calculations.[37] In this study we have also employed Grimme's dispersion correction (DFT+D3) as dispersive effects might be significant for the systems under investigation.[38] The 8x8 pristine graphene model is obtained from the bulk graphite structure with a calculated energy minimized lattice constant of a=b= 2.460 Å and c = 6.800 Å (Exp. A=b=2.461 Å and c = 6.709 Å).[39] For all our calculations, in the direction perpendicular to the surface we use a vacuum gap of ~15 Å, which is sufficient to eliminate any spurious interactions along the z-axis. The N-doped graphene model is obtained by the substitution of a C-atom on the pristine graphene. To understand the interaction of Pd-adatom with graphene in the presence of an O-containing organic functional group we graft an -OH group on the graphene surface. The choice to graft the graphene sheet with -OH group is to reduce the computational complexity.[40–42] Similarly, to model the preferred position of N in the presence of the -OH group we perform a series of calculations in which the substitution of N is done at different positions with respect to the -OH group (Supporting Note 2), which show that when the OH group on the neighboring C-atom has the lowest relative energy (Table S4). Therefore, the adsorption properties of Pd on -OH group N-doped graphene is studied on the model in which the OH group and the doped N-atoms are in the neighboring sites (Supporting Note 2, b). In addition to it the OH decorated pyrrolic graphene is modelled by creating a di-vacancy on the pristine graphene and by introducing a pyrrole ring. The three of the four dangling bonds are saturated using H-atoms and one of these dangling bonds is grafted with an -OH group. The dipole moment, due to the adsorption of the Pd adatom, is taken into account by using the methods implemented in VASP according to the procedures of Markov *et al.* and Neugebauer et al.[43,44] The charges on various atoms are obtained using the Bader charge analysis as implemented by Henkelman and coworkers.[45–47] The adsorption energy (E_{ad}) of the Pd adatom is calculated using:

$$E = E_{system+Pd} - E_{pristine\ system} - E_{Pd}, \quad \textbf{(1)}$$

where, $E_{system+Pd}$, $E_{pristine\ system}$ and E_{Pd} is the energy of Pd adsorbed on graphene, (pristine graphene, N-doped graphene, OH decorated graphene, OH decorated N-doped graphene, and OH decorated pyrrolic graphene) pristine surface and energy of the adatom respectively.

The electron charge density difference, ρ, is calculated using:

$$\rho = \rho_{\text{system+Pd}} - \rho_{\text{pristine system}} - \rho_{\text{Pd}}, \quad \textbf{(2)}$$

where, $\rho_{\text{system+Pd}}$, $\rho_{\text{pristine system}}$ and ρ_{Pd} is the charge density of Pd adsorbed on the above graphitic systems, pristine surface and energy of the adatom respectively.

Results and discussion

The formation of flake-like thin sheets of N-doped reduced graphene oxide to be used for Pd deposition was confirmed from microscopy analysis of the sample demonstrating the larger extent of exfoliation (Fig. S1a). High-resolution TEM images (HRTEM) displayed an inter-planar spacing of 0.35 nm corresponding to the (002) planes of turbostratic NRGO and selected area electron diffraction (SAED) pattern containing the characteristic features (Fig.s S1b,c). Nearly spherical 4 nm Pd NCs were deposited on the NRGO support *in-situ* by a solvothermal method at 200 ^{o}C using PVP as the reducing as well as capping agent (Fig. 1a, b). The corresponding particle-size distribution estimated by considering nearly 500 Pd particles is given in Fig. 1c. Careful observations in TEM confirmed that the particles are, as desirable, uniformly distributed over the NRGO sheets without forming clusters. A typical HRTEM image of a Pd particle in Fig. 1d shows the lattice fringes with an inter-planar spacing of 0.23 nm corresponding to the (111) planes of FCC Pd crystal. All diffraction rings in the SAED pattern (Fig. 1e) can be indexed on the pure FFC phase of Pd. Fig. 1f are the typical HAADF-STEM images with a high contrast for Pd confirming the homogeneous Pd loading on the NRGO sheets. We further performed EDS elemental mapping analysis on the same region to confirm a consistent distribution of C and N in the NRGO framework (Fig. 1g-i).

In order to understand the effect of nucleation of the Pd NCs on an NRGO or RGO surfaces *in-situ*, we synthesized the Pd/NRGO (*ex-situ*) by mixing pre-formed Pd NCs and NRGO. As seen in Fig. S2, the Pd NCs were agglomerated at places and sparsely placed on other areas on the NRGO surface. We believe the reason for such inhomogeneity is due to the weak interaction between the NRGO and pre-formed Pd NCs as compared to the shear forces present in the *ex-situ* deposition process leading to the clustering of the nanoparticles. In contrast, in the *in-situ* process, a larger concentration of the Pd(2+) ions surrounding the uniformly distributed electron-rich N centers of NRGO is expected, so that their 'on-the-spot' reduction to Pd(0) could arrest the clustering tendencies of the NCs. The N-Pd interactions were found to be prominent and decisive in delivering a high and stable electrocatalytic activity, as discussed later. The Pd/RGO sample prepared *in-situ* also yielded a uniform distribution of the Pd particles with an average size of 6 nm due to the interaction of the surface functional groups of RGO with Pd(2+) (Fig. S3). The comparison of the two

processes confirms that the *in-situ* deposition process has an advantage in offering a cluster-free deposition of the nanoparticles.

Powder X-ray diffraction patterns were recorded for all the samples in order to confirm the phase purity (Fig. 2 and Fig. S4). A diffraction peak at 10.5° for graphene oxide (GO) was observed for the (001) basal plane with a larger lattice spacing of 0.86 nm *vs.* graphite due to the presence of oxygen functionalities.[48] The same peak in RGO and NRGO shifted to 24.5° and 26.4° respectively as the functional groups were reduced during the synthesis process.[48] The peaks at 39.8°, 46.3°, 67.7° in Pd/NRGO *in-situ*, Pd/NRGO *ex-situ* and Pd/RGO *in-situ* are assigned to the (111), (200) and (220) crystal planes of palladium with FCC crystalline structure (JCPDS no. 88-2335) as shown in Fig. 2a. The peaks corresponding to Pd in both Pd/NRGO are broader as compared to Pd/RGO suggesting bigger particle size in the later, in good agreement with the TEM observation.

A detailed Raman spectral analysis was carried out to examine the Pd-substrate interactions and the effect of hetero-atom doping in the graphitic network. The spectra for GO, RGO, NRGO, Pd/RGO and Pd/NRGO exhibited two characteristic peaks at ~1360 cm^{-1} and ~1600 cm^{-1} respectively corresponding to the topological defects (D-band) and the crystalline graphitic regions (G-band) in all the samples (Fig. 2b and Fig. S5). The intensity ratio of the D and G bands for NRGO (1.03) is higher than GO (0.85) reveling the higher defect-density in the former due to the incorporation of N into graphene network (Fig. S5).[48] We also observed a red-shift of ~13 cm^{-1} in the G band in NRGO with respect to GO confirming the doping of heteroatom (Inset (i) in Fig. 2b).[48]

More importantly, when the D-bands of the NRGO were compared for bare and Pd/NRGO samples (*in-situ* and *ex-situ*), a prominent red-shift of the band (~20 cm^{-1}) was observed upon Pd loading (Inset (ii) in Fig. 2b). The D band position and intensity is carrier-density dependent, whose frequency increases for hole doping and decreases for electron doping.[49–51] This led us to believe that substantial electron transfer occurs from the Pd NCs to the graphene substrate, a bit more in the *in-situ* sample due to its higher D/G ratio. Such a shift was unremarkable in the Pd/RGO sample.

Evaluation of ORR performances: Generally, as the ORR activity is more facile at optimal metal loading on the substrates,[52–54] we first examined the effect of *in-situ* catalyst loading by using the Pd/NRGO samples with various Pd loading in the range of 22-47% (Fig. S6, 7). CV plots were recorded in Ar saturated 0.1 M KOH solution at a scan-rate of 50 mV/sec (Fig. 3a) and the corresponding ECSAs were determined by quantifying the charge transferred during the reduction of $Pd(OH)_2$ present on the catalyst surface.[55] The Pd oxide reduction peak of 22% loaded Pd/NRGO sample negatively shifted by 29 mV as compared to the 32% or 47% Pd loaded samples, indicating that the electronic structures of the surfaces changes upon

different Pd loading.[9] The ORR performances were evaluated in an O_2 saturated 0.1 M KOH solution using a GC RDE. As seen in Fig. 3b, the 22% and 47% Pd loaded samples have a nearly similar onset potential (1.0 V) whereas 32% loading exhibited a more favorable onset value (~ 1.06 V). At higher potentials, the diffusion limited current attained a value of ~ 5.6 mA/cm^2, close to the theoretical one (~5.7 mA/cm^2)[56,57] for all samples indicating a minimal contribution from O_2 diffusion.[6] The O_2 mass-transfer dependent ORR currents in the intermittent potential range were compared from the half-wave potential ($E_{1/2}$). The $E_{1/2}$ values were in the order of 22% (0.85 V)<47%(0.88 V) <32%(0.93 V) of Pd-loading (Fig. 3b) suggesting that with increasing Pd content on NRGO, ORR activity improves initially until ~ 32% loading and decreases thereafter. Furthermore, the ORR kinetic currents for these samples at 0.9 V (*vs.* RHE) obtained from Koutecky–Levich (K-L) equation were normalized with the electrochemically active surface area (ECSA) and Pd mass (specific activity, $I_{k,specific}$ and mass-activity, $I_{k,mass}$ respectively, see Supplementary Note-1 and Fig. S8-10) as given in Table 1 to show a high activity at 32% loading.

To scrutinize the effect of *in-situ* loading and the Pd-N interactions, we recorded the ORR polarization curves for a 32% Pd loaded Pd/NRGO sample prepared *in-situ & ex-situ*, 32% Pd/RGO sample prepared *in-situ*, NRGO and commercial 40 wt.% Pt/C (Fig. 3c). The Pd/NRGO and the Pd/RGO samples have comparable onset potential whereas Pt/C has a noticeably lower value (~ 30 mV). On the other hand, the $E_{1/2}$ in these samples decreased in the order of Pd/NRGO *in-situ* (0.93V)>Pd/NRGO *ex-situ* (0.90 V)> Pd/RGO (0.86 V) ~ Pt/C (0.86 V). The ORR performance of NRGO is quite poor. The ECSA obtained from the CV plots in Fig. 3d showed the highest value for the Pd/NRGO *in-situ* sample (15 m^2/g) as compared to the Pd/NRGO *ex-situ* (13.1 m^2/g, probably due to random agglomeration of the Pd NCs seen in Fig. S2) and Pt/C (11.7 m^2/g). The mass and specific activities for all the samples were calculated from the K-L plots given in Fig. S8, 11-13. The Pd/NRGO *in-situ* sample produced the highest $I_{k,mass}$ of 0.59 A/mg, ~5 times better than the commercial Pt/C (0.12 A/mg) (Fig. 3e, Table 1). In comparison, $I_{k,mass}$ of the Pd/NRGO *ex-situ* sample is only 0.25 A/mg, suggesting that the method of *in-situ* deposition plays a crucial role in delivering improved ORR kinetics. Similarly, $I_{k,specific}$ for the samples showed a similar trend with 3.96 mA/cm^2 for the Pd/NRGO *in-situ* which is 1.8 higher than the Pd/NRGO *ex-situ* (1.94 mA/cm^2 (Fig. S14). Furthermore, the $I_{k,mass}$ for the Pd/NRGO *in-situ* is ~4 times higher than the Pd/RGO, indicating the crucial role of N present in graphene sheets for an improved reduction kinetics (Fig. 3e). From these findings and a comprehensive comparison with the other recently developed Pd-based catalysts, the performance of Pd/NRGO *in-situ* (32% loading) sample was found to be fairly superior (Table S1).

Stability and methanol tolerance tests: The Pd/NRGO *in-situ* sample exhibited very high stability and methanol tolerance. We have compared its stability with that for the Pd/RGO and the commercial Pt/C through CV cycling between 0.6 V-1.1 V *vs.* RHE in O_2 saturated 0.1 M KOH at a sweep rate of 100 mV

s^{-1}. Fig. 4a, b show the LSV plots of the Pd/NRGO *in-situ* and the commercial Pt/C acquired before and after the stability test. The $E_{1/2}$ of the Pd/NRGO *in-situ* reduced by only 10 mV and 13 mV after 10000 and 15000 CV cycles respectively. On the other hand, Pt/C experienced a decrease of 100 mV and 108 mV after as many cycles. The $I_{k,mass}$ of the Pd/NRGO *in-situ* became 0.47 A/mg (20% loss) and 0.42 A/mg (28% loss) after 10000 and 15000 CV cycles respectively while Pt/C showed a 60% and 72% decrease in the same period (Fig. 4c). The corresponding decrease in the $I_{k,specific}$ after 15000 cycles was 14% and 47% of the initial value for the Pd/NRGO *in-situ* and the Pt/C respectively (Fig. 4d). The disparity between the mass and specific activity may be due to loss of catalyst from the electrode, somewhat compounded by the Pd surface activation, as analysis of the intermittent cycles show that after 5000 CV cycle, the $E_{1/2}$ of the Pd/NRGO *in-situ* showed a positive shift of 8 mV (Fig. S15).[58] The stability of the Pd/RGO was rather poor and exhibited a shift of 35 mV in $E_{1/2}$ after 1000 cycles, suggesting a crucial role of nitrogen in the graphene network in imparting high electrochemical stability (Fig. S16).

The samples after accelerated durability test were examined under TEM (Fig. S17 and S18). The Pd/NRGO *in-situ* has maintained a nearly uniform distribution of the Pd NCs. On the other hand, agglomeration of the Pd NCs was observed in Pd/RGO, indicating that an improved stability of the Pd/NRGO *in-situ* was due to a strong catalyst-support bonding that minimizes the surface migration of Pd NCs to form agglomerates.

For the methanol (MeOH) tolerance test, electrocatalytic methanol oxidation behavior of the Pd/NRGO *in-situ* and the Pt/C were first examined by recording CVs in Ar saturated 0.1 M KOH + 0.1 M MeOH as shown in Fig. 5a. MeOH oxidation peak current for Pt/C was ~3 times higher suggesting, as desired, a poorer electrocatalytic activity of Pd/NRGO *in-situ* towards methanol oxidation. The ORR polarization curves recorded before and after the addition of methanol is given in Fig. 5b. The $E_{1/2}$ remains unchanged for Pd/NRGO in presence or absence of MeOH while in the case of Pt/C, $E_{1/2}$ is negatively shifted by 0.11 V in presence of MeOH. Similarly, MeOH added during the chronoamperometric measurements also showed a drastic change in the current density of the Pt/C (68% loss) while Pd/NRGO *in-situ* suffered only a minute loss even after 1000 s (Fig. 5c). Overall, the activity, stability and methanol tolerance studies reflect that the *in-situ* prepared Pd/NRGO (32% loading) with a uniform dispersion of the Pd NCs and their interaction with N of graphene framework acts as an excellent ORR electrocatalysts in alkaline medium.[59]

Origin of enhanced catalytic activity and stability: As Raman studies indicated a profound metal→substrate electron transfer, hard X-ray photoelectron spectroscopy (HAXPES) was employed to assess the nature and the composition of the elements in the Pd/NRGO *in-situ*. The survey spectrum in Fig. S19a shows the presence of Pd, C, N, and O in the sample with an estimated Pd and N content of 31.8 wt%

and 7.1 wt% respectively. We investigated the chemical states of C, N, and Pd therein from the corresponding high-resolution (HR) HAXPES spectra. The HR-HAXPES spectra of C is given in Fig. S19b. Deconvolution of the C 1*s* peak revealed 3 different components arising from C-sp^2 (284.5 eV), C-sp^3 (285.6 eV), and C atoms attached to N (287.0 eV).[48,60,61] Since N content is only 7.1%, the peak corresponding to the C-N interaction has the least contribution among the three (Fig. S19c). The N 1*s* peak shows the presence of three different N functionalities which can be attributed to the pyridinic, pyrrolic and graphitic nitrogen corresponding to the peaks at 398.3 eV, 399.8 eV, 400. 9 eV respectively as given in Fig. S19d.[48,62] Pyridinic and pyrrolic forms contribute ~81% of the total N content and believed to be responsible, as discussed later, for coordinating with Pd to improve the structural stability of the composite material during electrocatalysis (Fig. S19e).[48]

Theoretical studies have recently proposed that oxygen binds more strongly to Pd as compared to Pt[63] which causes an easy cleavage of the O-O bond on the Pd surface but a slow desorption of the oxygenated intermediates.[64–66] Therefore by reducing electron density on Pd, it should be possible to improve the ORR kinetics significantly.[66,67] In order to understand the improved ORR kinetics and the role played by N in the Pd/NRGO, we further compared the HAXPES data for the *in-situ* deposited sample and the *ex-situ* deposited components. The Pd 3*d* core-level and N 1*s* HAXPES peaks of the bare Pd NCs, NRGO and Pd/NRGO *in-situ* samples are plotted in Fig. 6. The Pd 3*d* binding energy of Pd/NRGO *in-situ* shifted positively as compared to the bare Pd NCs by ~ 0.18 eV (Fig. 6a) suggesting a transfer of Pd *d*-electron to NRGO sheets resulting in a reduced Pd electron density in the composite as compared to the bare NCs. Concomitantly the binding energy for the pyrrolic N in N 1*s* spectrum was shifted prominently (0.22 eV) to a lower energy as compared to that in the pure NRGO (Fig. 6b) while the changes in the binding energies of the pyridinic and graphitic N remained unremarkable. Moreover, there was a change in the abundance ratio of the three nitrogen moieties in the two samples (Fig. S20) indicating an interesting Pd mediated rearrangement in the graphene network. The shift in the N peak confirms that the Pd is bound to the NRGO primarily via the pyrrolic N. As pyrrolic N is more electronegative and the lone pair of electron is less available (as it is in conjugation), it has the ability to withdraw electron density from Pd as compared to the graphitic or pyridinic N and induces a downshift of the *d*-band center of Pd for superior ORR.[30,64,66,67] Moreover, the strong bonding of Pd with NRGO also gives rise to its highly improved stability during 15000 electrocatalytic cycles by arresting leaching or surface migration of Pd.[21,68]

To clarify the reasons behind a better performance of Pd on NRGO and the nature of charge-transfer between them, we performed DFT calculations on the adsorption of Pd adatom on pristine graphene (G), graphitic N-doped graphene (N_G), OH decorated graphene (G_{OH}), OH decorated graphitic N-doped graphene ($N_{G\text{-}OH}$), and OH decorated pyrrolic N-doped graphene ($N_{Pyr\text{-}OH}$). We considered only pyrrolic N

since our experiments showed that pyridinic and graphitic N moieties retained, more or less, their pristine electronic structure upon Pd loading. OH was selected as the simplest representative oxygen containing group and also, as the experiments were carried out in an OH rich medium. The Pd adatoms were allowed to be adsorbed on different sites of the above-mentioned systems and then they were fully relaxed. The perspective views of the relaxed structures of all these systems have been provided in Fig. S21-25. For clarity, the most stable structures of each of these systems, as indicated by the calculated adsorption energies have been presented in Fig. 7 (Table S2 and S3). The calculations show that the Pd adatom is most stable on the bridge sites, as seen in previous studies[29] and the adsorption is most negative (meaning most stable) in the case the $N_{Pyr\text{-}OH}$, as anticipated from the experimental observations. Notably the Pd binding is accompanied by a change in the planarity of the graphene sheet that occurs locally at the sites where Pd and the OH groups have been grafted. Such a geometrical change was found to be more pronounced in the case of the $N_{Pyr\text{-}OH}$ due to a stronger interaction with the Pd-atom. Accordingly, the dihedral angle of the graphene layer away from the Pd absorption site was found to be only ~0.417° for pristine graphene, while it is ~1.037° for the $N_{Pyr\text{-}OH}$. Note that the same may be also contributed by strain due to a repulsive interaction between the OH group and the H-atoms in the active site.

To better understand the underlying reasons for the higher stability of Pd on the $N_{Pyr\text{-}OH}$ system, we investigated the density of states. As shown in Fig. S26, the overall shape of the total density of states (tDOS) signatures of pristine graphene, Pd/G and Pd/$N_{Pyr\text{-}OH}$ are very similar. The probable reason for such similarity may be associated with the fact that major contribution to tDOS is from the C atoms. However, in the Pd/$N_{Pyr\text{-}OH}$ system, we can see asymmetric semi-localised π states in the vicinity of the Fermi energy (E_F), which are due to the creation of the di-vacancy on the pristine graphene to model pyrrolic graphene giving rise to magnetic behaviour.[69] To further investigate the stability of Pd on the $N_{Pyr\text{-}OH}$ system we compared its partial density of states (PDOS) with Pd on pristine graphene. We note that in the $N_{Pyr\text{-}OH}$ system there is no direct interaction of the Pd atom with the C framework and therefore, the C *p*-orbital signatures were not considered. As seen in Fig. 8a, b, it was found that post-adsorption, the highly localized *d*-orbital signatures of the Pd adatom, the C *p*-orbitals of pristine graphene (Fig. 8a) and N *p*-orbital and O *p*-orbitals of $N_{Pyr\text{-}OH}$ (Fig. 8b) move to lower energy to cross and overlap with each other, asserting the formation of chemical bonds between the interacting atoms (Fig. S27). A careful analysis of these signatures shows an interesting overlapping region (green dotted rectangle Fig. 8a, b) between the Pd *d*-orbitals and the C *p*-orbital signatures in pristine graphene occurring between -8.472 eV to -3.605 eV while in the $N_{Pyr\text{-}OH}$ the overlap of Pd *d*-orbital and N and O *p*-orbital signatures is in between -10.421 eV to -3.253 eV. Clearly, the area under the curve of the overlapping region for the later system is much larger inferring that the chemical bonding is stronger, leading to its higher stability. The Bader charge analysis on the above systems show that the charge on Pd attached to pristine graphene and $N_{Pyr\text{-}OH}$ are 0.179 e and

0.291 e respectively. Thus, while there is electron transfer from Pd-adatom on both the systems it is higher for those adsorbed on the $N_{Pyr\text{-}OH}$. The charge-density difference can be clearly visualized in Fig. 8c, d to demonstrate that the interaction of Pd *d*-orbitals with N and O *p*-orbitals agrees well with the PDOS analysis. Additionally, it shows the depletion of electron density around the Pd atom agreeing with the Bader charge analysis. Therefore, we conclude that the adsorption of Pd on the $N_{Pyr\text{-}OH}$ should exhibit better electrocatalytic performance, as observed experimentally, as compared to the other graphene systems considered here due to stronger chemical bonding accompanied with a relatively higher charge-transfer.

The overall enhancement in activity and stability of Pd/NRGO *in-situ vs*. Pd/NRGO *ex-situ* or Pd/RGO or Pt/C or Pd/C is attributed to the following three factors. (1) The *in-situ* deposition process enables uniform deposition of Pd NCs on NRGO without obvious agglomeration benefiting the surface reactions with high ECSA, (2) the pyrollic-N moieties in NRGO strongly interacts with Pd NCs by withdrawing its electron cloud, and (3) arresting surface migration of Pd due to the strong interaction lending high electrocatalytic stability.

Conclusions

In conclusion, we have been able to realize highly active and durable electrocatalysts for oxygen reduction reaction in alkaline conditions by using Pd nanocrystals deposited in an atom-by-atom fashion on N-doped reduced graphene oxide support. The *in-situ* deposition on carbon is better than deposition of pre-formed nanocrystals due to minimal effect of the shear-forces acting during deposition. We found that among the different nitrogen moieties, pyrrolic-N forms a strong bond with Pd and induces a facile metal to carbon charge-transfer, while it is usually the pyridinic-N that have been shown to participate in a similar fashion in ORR in the previous studies. The ORR activity and durability of these Pd nanocrystals is better than those generated from the pyridinic-N-Pd bonds and has been attributed to the delocalization of the Pd 3*d*-electrons over the 2*p* orbitals of N, C and O (of the neighboring functional group) accompanied by a slight deformation of the graphene planar structure around this bond. Since N-doping creates large quantities of pyrrolic-N in graphene, the use of its bonding with a metal should help to generate many active and stable electrocatalysts.

Acknowledgements

LS thank UGC for the research fellowship. SM is grateful to MHRD, India for fellowship. The central facilities at IISER Mohali are gratefully acknowledged. Part of the experiment were carried out at the light source PETRA III of DESY, a member of the Helmholtz Association (HGF).

References

1 X. Ge, A. Sumboja, D. Wuu, T. An, B. Li, F. W. T. Goh, T. S. A. Hor, Y. Zong and Z. Liu, *ACS Catal.*, 2015, **5**, 4643–4667.

2 M. Shao, Q. Chang, J.-P. Dodelet and R. Chenitz, *Chem. Rev.*, 2016, **116**, 3594–3657.

3 Y. Zhang, B. Huang, Q. Shao, Y. Feng, L. Xiong, Y. Peng and X. Huang, *Nano Lett.*, 2019, **19**, 6894–6903.

4 H. Zhang, X. Qiu, Y. Chen, S. Wang, S. E. Skrabalak and Y. Tang, *Small*, 2020, **16**, 1906026.

5 M. Rana, S. Mondal, L. Sahoo, K. Chatterjee, P. E. Karthik and U. K. Gautam, *ACS Appl. Mater. Interfaces*, 2018, **10**, 33737–33767.

6 Y. Lu, Y. Jiang, X. Gao, X. Wang and W. Chen, *J. Am. Chem. Soc.*, 2014, **136**, 11687–11697.

7 K. Jiang, P. Wang, S. Guo, X. Zhang, X. Shen, G. Lu, D. Su and X. Huang, *Angew. Chemie Int. Ed.*, 2016, **55**, 9030–9035.

8 C. Li, Q. Yuan, B. Ni, T. He, S. Zhang, Y. Long, L. Gu and X. Wang, *Nat. Commun.*, 2018, **9**, 1–9.

9 Y. Wang and A. S. Hall, *ACS Energy Lett.*, 2020, **5**, 17–22.

10 B. K. Barman, 2019, **2**, 13928–13931.

11 X. Lu, M. Ahmadi, F. J. Disalvo and H. D. Abruña, *ACS Catal.*, 2020, **10**, 5891–5898.

12 Y. Rao, C. Cai, J. Tan and M. Pan, *J. Electrochem. Soc.*, 2019, **166**, F351–F356.

13 Y. Yang, G. Chen, R. Zeng, A. M. Villarino, F. J. Disalvo, R. B. Van Dover and H. D. Abruña, *J. Am. Chem. Soc.*, 2020, **142**, 3980–3988.

14 J. T. L. Gamler, K. Shin, H. M. Ashberry, Y. Chen, S. L. A. Bueno, Y. Tang, G. Henkelman and S. E. Skrabalak, *Nanoscale*, 2020, **12**, 2532–2541.

15 L. B. Venarusso, C. V. Boone, J. Bettini and G. Maia, *J. Mater. Chem. A*, 2018, **6**, 1714–1726.

16 J. Greeley, I. E. L. Stephens, A. S. Bondarenko, T. P. Johansson, H. A. Hansen, T. F. Jaramillo, J. Rossmeisl, I. Chorkendorff and J. K. Nørskov, *Nat. Chem.*, 2009, **1**, 552–556.

17 V. R. Stamenkovic, B. S. Mun, M. Arenz, K. J. J. Mayrhofer, C. A. Lucas, G. Wang, P. N. Ross and N. M. Markovic, *Nat. Mater.*, 2007, **6**, 241–247.

18 S. Liu, Q. Zhang, Y. Li, M. Han, L. Gu, C. Nan, J. Bao and Z. Dai, *J. Am. Chem. Soc.*, 2015, **137**, 2820–2823.

19 C. Wu, H. Li, H. He, Y. Song, C. Bi, W. Du and H. Xia, *ACS Appl. Mater. Interfaces*, 2019, **11**, 46902–46911.

20 W. Xiao, M. A. Liutheviciene Cordeiro, M. Gong, L. Han, J. Wang, C. Bian, J. Zhu, H. L. Xin and D. Wang, *J. Mater. Chem. A*, 2017, **5**, 9867–9872.

21 C. Lafforgue, F. Maillard, V. Martin, L. Dubau and M. Chatenet, *ACS Catal.*, 2019, 5613–5622.

22 E. Rangel, L. F. Magana and L. E. Sansores, *ChemPhysChem*, 2014, **15**, 4042–4048.

23 X. Liu, L. Li, C. Meng and Y. Han, *J. Phys. Chem. C*, 2012, **116**, 2710–2719.

24 Y. Tian, Y. J. Liu, J. X. Zhao and Y. H. Ding, *RSC Adv.*, 2015, **5**, 34070–34077.

25 Z. Bao, H. Zhou, X. Song, Y. Gao, G. Zhuang, S. Deng, Z. Wei, X. Zhong and J. Wang, *ChemCatChem*, 2019, **11**, 1278–1285.

26 X. Jiang, T. Huang, G. Fu, J. M. Lee, X. Jiang, J. Wang, Y. Tang, X. Qiu, X. Jiang and J. Zhou, *J. Mater. Chem. A*, 2019, **7**, 26243–26249.

27 R. Arrigo, M. E. Schuster, Z. Xie, Y. Yi, G. Wowsnick, L. L. Sun, K. E. Hermann, M. Friedrich, P. Kast, M. Hävecker, A. Knop-Gericke and R. Schlögl, *ACS Catal.*, 2015, **5**, 2740–2753.

28 Z. He, B. Dong, W. Wang, G. Yang, Y. Cao, H. Wang, Y. Yang, Q. Wang, F. Peng and H. Yu, *ACS Catal.*, 2019, **9**, 2893–2901.

29 D. A. Bulushev, M. Zacharska, E. V. Shlyakhova, A. L. Chuvilin, Y. Guo, S. Beloshapkin, A. V. Okotrub and L. G. Bulusheva, *ACS Catal.*, 2016, **6**, 681–691.

30 L. M. Ombaka, P. G. Ndungu and V. O. Nyamori, *RSC Adv.*, 2015, **5**, 109–122.

31 A. Ejaz and S. Jeon, *Int. J. Hydrogen Energy*, 2018, **43**, 5690–5702.

32 P. Wang, X. Shi, C. Fu, X. Li, J. Li, X. Lv, Y. Chu, F. Dong and G. Jiang, *Nanoscale*, 2020, **12**, 843–850.

33 H. Jiang, L. Liu, K. Zhao, Z. Liu, X. Zhang and S. Hu, *Electrochim. Acta*, 2020, **337**, 135758.

34 Schulueter C.; Gloskovskii A.; Ederer K.; Schostak I.; Piec S.; Sarkar I.; Matveyev Y.; Lömker P.; Sing M.; Claessen R.; Wiemann C.; M.Schneider C.; Medjanik K.; Schönhense G.; Amann P.;

Nilsson A.; Drube W. AIP conference proceedings 2019, 2054, 040010-040016..

35 G. Kresse and J. Furthmüller, *Phys. Rev. B*, 1996, **54**, 11169–11186.

36 P. E. Blöchl, *Phys. Rev. B*, 1994, **50**, 17953–17979.

37 J. P. Perdew, A. Ruzsinszky, G. I. Csonka, O. A. Vydrov, G. E. Scuseria, L. A. Constantin, X. Zhou and K. Burke, *Phys. Rev. Lett.*, 2008, **100**, 136406-1-136406–4.

38 S. Grimme, J. Antony, S. Ehrlich and H. Krieg, *J. Chem. Phys.*, 2010, **132**.

39 M. T. Yin and M. L. Cohen, *Phys. Rev. B*, 1984, **29**, 6996–6998.

40 A. Chutia, F. Cimpoesu, H. Tsuboi and A. Miyamoto, *Chem. Phys. Lett.*, 2011, **503**, 91–96.

41 A. Chutia, I. Hamada and M. Tokuyama, *Surf. Sci.*, 2014, **628**, 116–125.

42 A. Chutia, R. Sahnoun, R. C. Deka, Z. G. Zhu, H. Tsuboi, H. Takaba and A. Miyamoto, *Phys. B-Condensed Matter*, 2011, **406**, 1665–1672.

43 G. Makov and M. Payne, *Phys. Rev. B*, 1995, **51**, 4014–4022.

44 J. Neugebauer and M. Scheffler, *Phys. Rev. B*, 1992, **46**, 16067–16080.

45 E. Sanville, S. D. Kenny, R. Smith and G. Henkelman, *J. Comput. Chem.*, 2007, **28**, 899–908.

46 W. Tang, E. Sanville and G. Henkelman, *J. Phys. Condens. Matter*, 2009, **21**, 084204.

47 G. Henkelman, A. Arnaldsson and H. Jónsson, *Comput. Mater. Sci.*, 2006, **36**, 354–360.

48 X. Zhang, J. Zhu, C. S. Tiwary, Z. Ma, H. Huang, J. Zhang, Z. Lu, W. Huang and Y. Wu, *ACS Appl. Mater. Interfaces*, 2016, **8**, 10858–10865.

49 J. Liu, Q. Li, Y. Zou, Q. Qian, Y. Jin, G. Li, K. Jiang and S. Fan, *Nano Lett.*, 2013, **13**, 6170–6175.

50 M. Bruna, A. K. Ott, M. Ijäs, D. Yoon, U. Sassi and A. C. Ferrari, *ACS Nano*, 2014, **8**, 7432–7441.

51 R. Beams, L. Gustavo Cançado and L. Novotny, *J. Phys. Condens. Matter*, 2015, **27**, 83002.

52 A. Kriston, T. Xie, P. Ganesan and B. N. Popov, *J. Electrochem. Soc.*, 2013, **160**, F406–F412.

53 D. Bhalothia, C.-Y. Lin, C. Yan, Y.-T. Yang and T.-Y. Chen, *Sustain. Energy Fuels*, 2019, **3**, 1668–1681.

54 S. Taylor, E. Fabbri, P. Levecque, T. J. Schmidt and O. Conrad, *Electrocatalysis*, 2016, **7**, 287–

296.

55 M. H. Seo, S. M. Choi, H. J. Kim and W. B. Kim, *Electrochem. commun.*, 2011, **13**, 182–185.

56 K. J. J. Mayrhofer, D. Strmcnik, B. B. Blizanac, V. Stamenkovic, M. Arenz and N. M. Markovic, *Electrochim. Acta*, 2008, **53**, 3181–3188.

57 Y. Garsany, O. A. Baturina, K. E. Swider-Lyons and S. S. Kocha, *Anal. Chem.*, 2010, **82**, 6321–6328.

58 K. A. Kuttiyiel, K. Sasaki, G. G. Park, M. B. Vukmirovic, L. Wu, Y. Zhu, J. G. Chen and R. R. Adzic, *Chem. Commun.*, 2017, **53**, 1660–1663.

59 L. Lu, Z. Wang, S. Zou, Y. Zhou, W. Hong, R. Li, L. Xiao, J. Liu, X. Q. Gong and J. Fan, *J. Mater. Chem. A*, 2018, **6**, 18884–18890.

60 Y. Wang, Y. Shao, D. W. Matson, J. Li and Y. Lin, *ACS Nano*, 2010, **4**, 1790–1798.

61 L. Perini, C. Durante, M. Favaro, V. Perazzolo, S. Agnoli, O. Schneider, G. Granozzi and A. Gennaro, *ACS Appl. Mater. Interfaces*, 2015, **7**, 1170–1179.

62 L. Sun, B. Liao, X. Ren, Y. Li, P. Zhang, L. Deng and Y. Gao, *Electrochim. Acta*, 2017, **235**, 543–552.

63 Y. Sha, T. H. Yu, B. V Merinov and W. A. Goddard, *ACS Catal.*, 2014, **4**, 1189–1197.

64 F. H. B. Lima, J. Zhang, M. H. Shao, K. Sasaki, M. B. Vukmirovic, E. A. Ticianelli and R. R. Adzic, *J. Phys. Chem. C*, 2007, **111**, 404–410.

65 V. R. Stamenkovic, B. Fowler, B. S. Mun, G. Wang, P. N. Ross, C. A. Lucas and N. M. Marković, *Science (80-.).*, 2007, **315**, 493 LP – 497.

66 M. H. Seo, S. M. Choi, J. K. Seo, S. H. Noh, W. B. Kim and B. Han, *Appl. Catal. B Environ.*, 2013, **129**, 163–171.

67 A. Sarkar, A. V. Murugan and A. Manthiram, *J. Mater. Chem.*, 2009, **19**, 159–165.

68 S. Kabir, A. Zadick, P. Atanassov, L. Dubau and M. Chatenet, *Electrochem. commun.*, 2017, **78**, 33–37.

69 I. A. Pašti, A. Jovanović, A. S. Dobrota, S. V Mentus, B. Johansson and N. V Skorodumova, *Phys. Chem. Chem. Phys.*, 2018, **20**, 858–865.

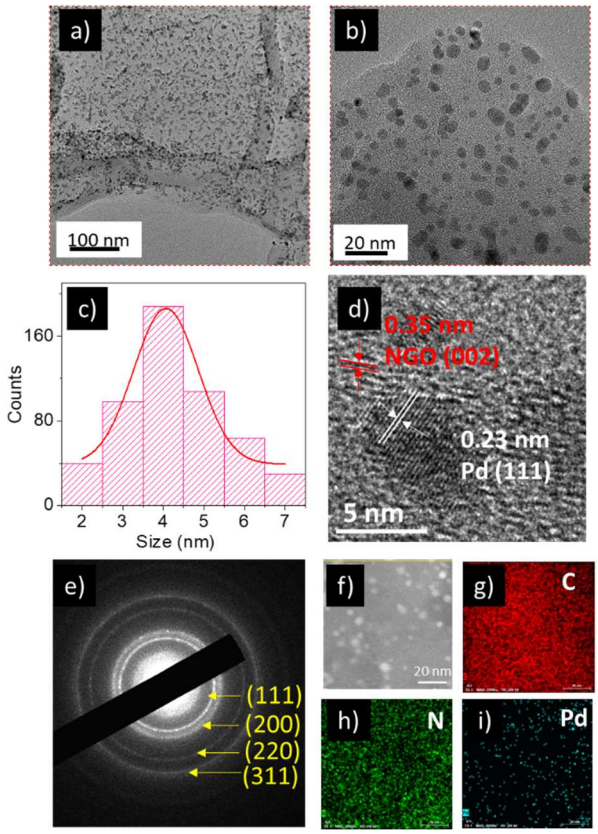

Fig. 1 Microscopic characterization of Pd/NRGO *in-situ* (32% loading) sample, (a, b) typical TEM images, (c) the particle-size distribution, (d) high-resolution TEM, (e) corresponding SAED pattern, (f) HAADF-STEM images and (g-i) corresponding energy dispersive X-ray spectroscopic elemental mapping images.

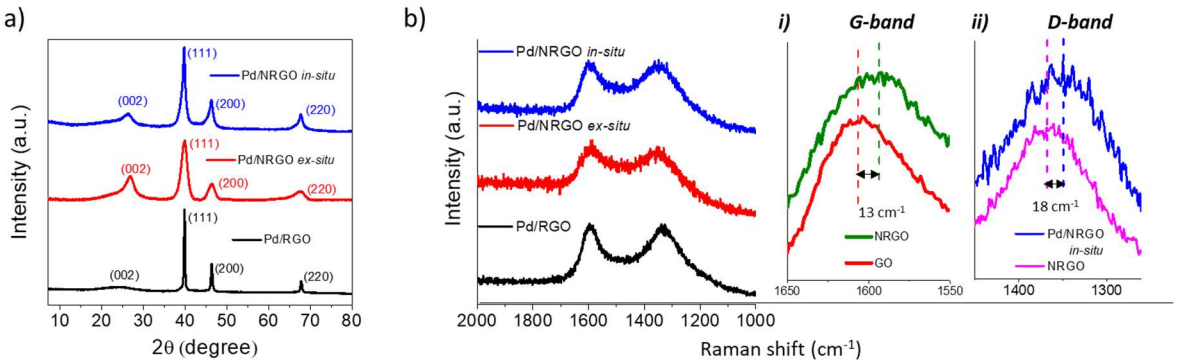

Fig. 2 a) Powder XRD patterns and b) Raman spectra of the Pd/NRGO *in-situ*, Pd/NRGO-*ex-situ* and Pd/RGO samples (all 32% Pd loading). Insets (i) and (ii) in (b) highlight the relative shifts in the respective Raman bands.

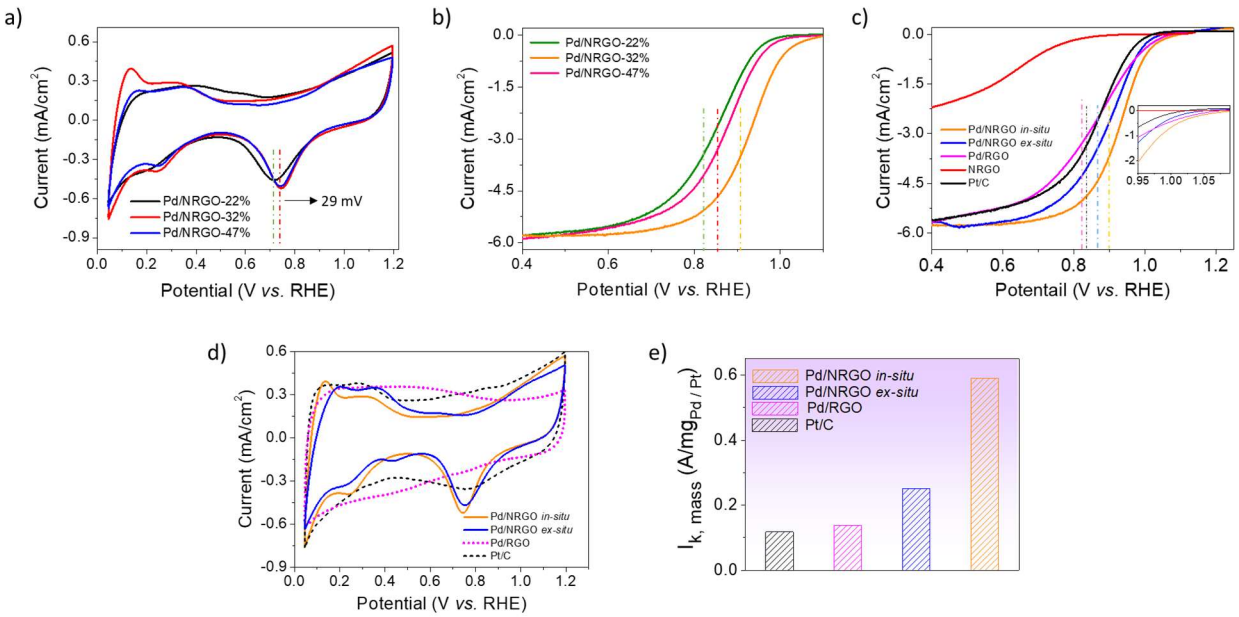

Fig. 3 Electrochemical characterization. a) Cyclic voltammograms of the Pd/NRGO (*in-situ*) samples with different Pd loading recorded in Ar saturated 0.1 M KOH with a scan-rate of 50 mV/s. b) The ORR polarization curves of (b) the different Pd/NRGO *in-situ* samples and c) the Pd/NRGO *in-situ* (32% loading), Pd/NRGO *ex-situ* (32% loading), Pd/RGO (32% loading), NRGO and commercial Pt/C (40% loading) recorded in O_2 saturated 0.1 M KOH at a scan-rate of 10 mV/s, d) CVs for the Pd/NRGO *in-situ*, Pd/NRGO *ex-situ*, Pd/RGO (all 32% loading) and Pt/C recorded in Ar saturated 0.1 M KOH with scan-rate of 50 mV/s, e) mass activities of Pd/NRGO *in-situ*, Pd/NRGO *ex-situ*, Pd/RGO (all 32% loading), and commercial Pt/C at 0.9 V *vs.* RHE.

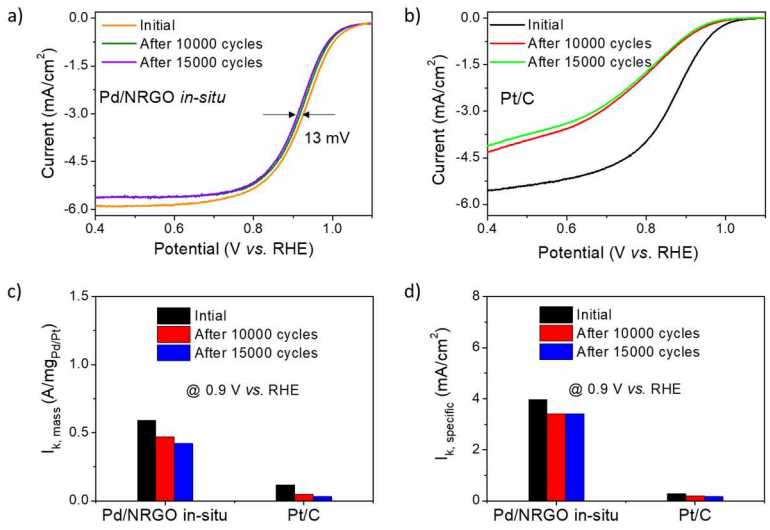

Fig. 4 a, b) ORR polarization curves of Pd/NRGO *in-situ* sample (32% loading) and commercial Pt/C before and after durability tests in O_2 saturated 0.1 M KOH at 1600 rpm and c,d) the corresponding mass and specific activities.

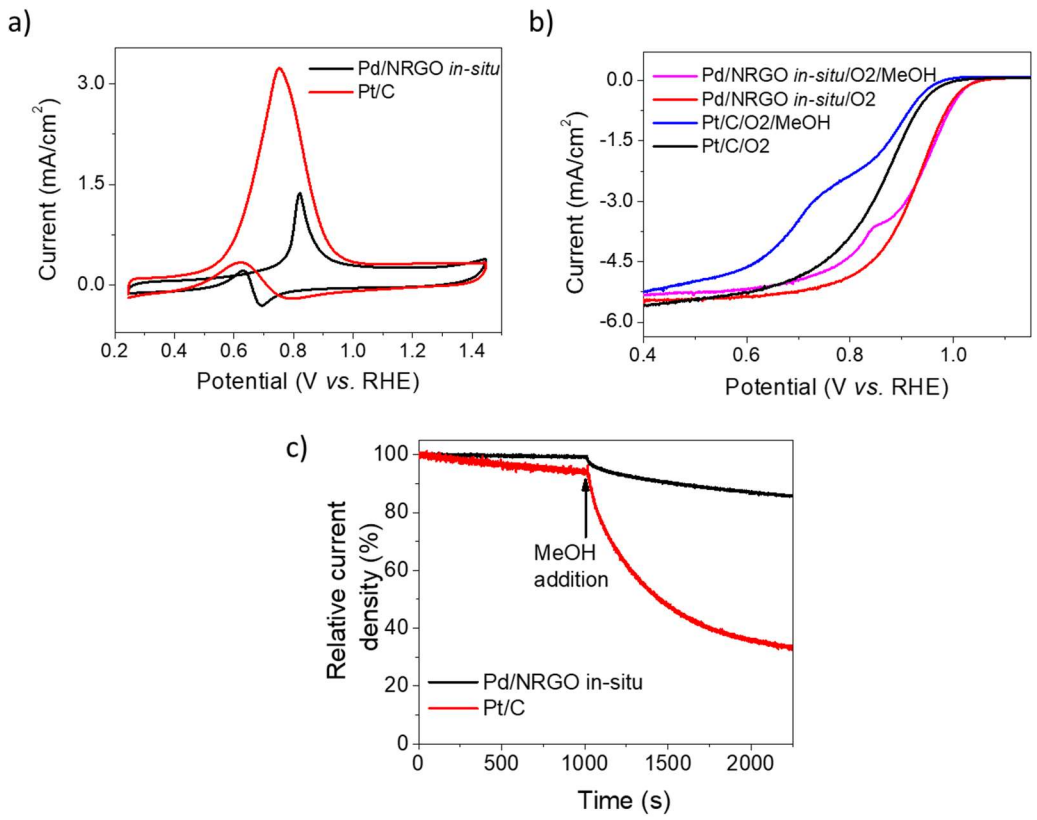

Fig. 5 a) Cyclic voltammograms of Pd/NRGO *in-situ* (32% loading) and commercial Pt/C in Ar saturated 0.1 M KOH + 0.1 methanol solution at a scan-rate of 50 mV/s, b) ORR polarization curves of the same Pd/NRGO *in-situ* and Pt/C in O_2 saturated 0.1 M KOH before and after adding methanol with an effective concentration of 0.1 M, c) chronoamperometry plots for the samples in O_2 saturated 0.1 M KOH before and after adding methanol with an effective concentration of 0.1 M (at 1000 s).

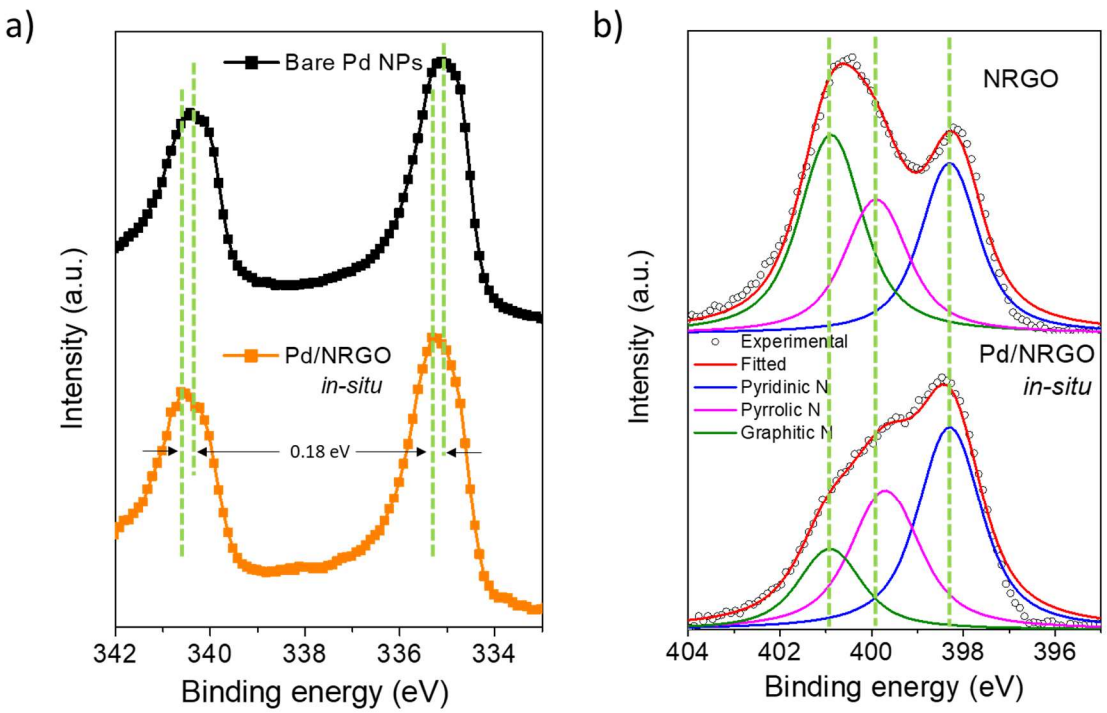

Fig. 6 a) HAXPES spectra of Pd 3*d* core level of Pd NCs and Pd/NRGO *in-situ* sample (32% loading), b) HAXPES spectra of N 1*s* of NRGO and Pd/NRGO *in-situ* sample. The green dotted lines are the guide to the eye for comparing peak positions.

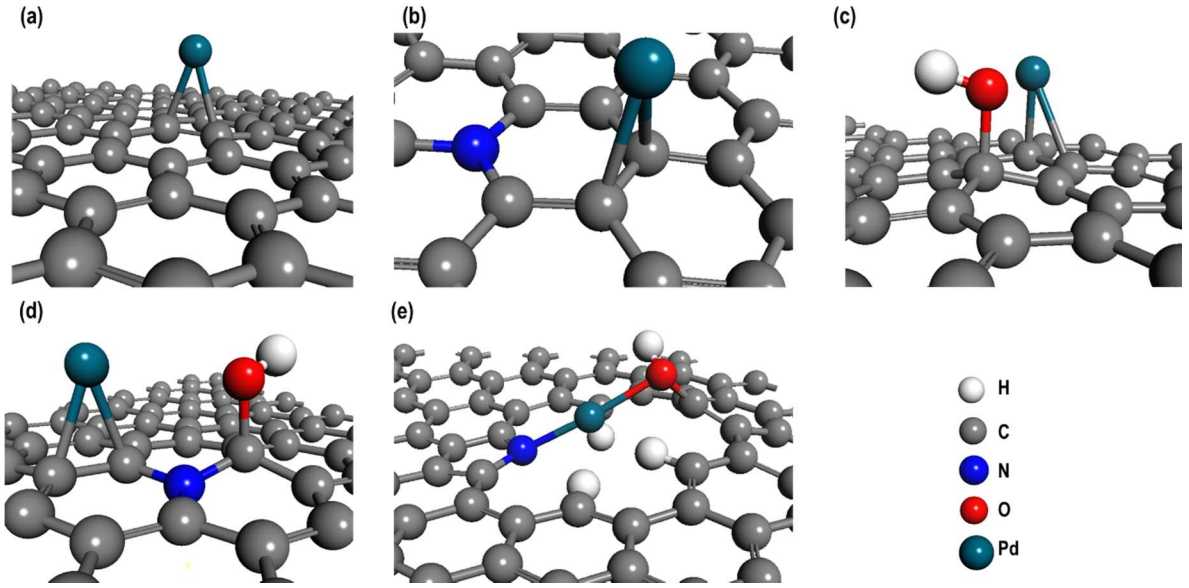

Fig. 7 The fully relaxed and the most stable structures of Pd adatom adsorbed on (a) pristine graphene (G, E_{ad}=-1.699 eV), (b) NG (E_{ad} = -1.709 eV), (c) G_{OH} (E_{ad}=-2.039 eV), (d) $N_{G\text{-}OH}$ (E_{ad} = -1.750 eV), and (e) $N_{Pyr\text{-}OH}$(E_{ad} = -2.516 eV). For clarity the active sites have been zoomed-in and the periodic boundaries have been omitted.

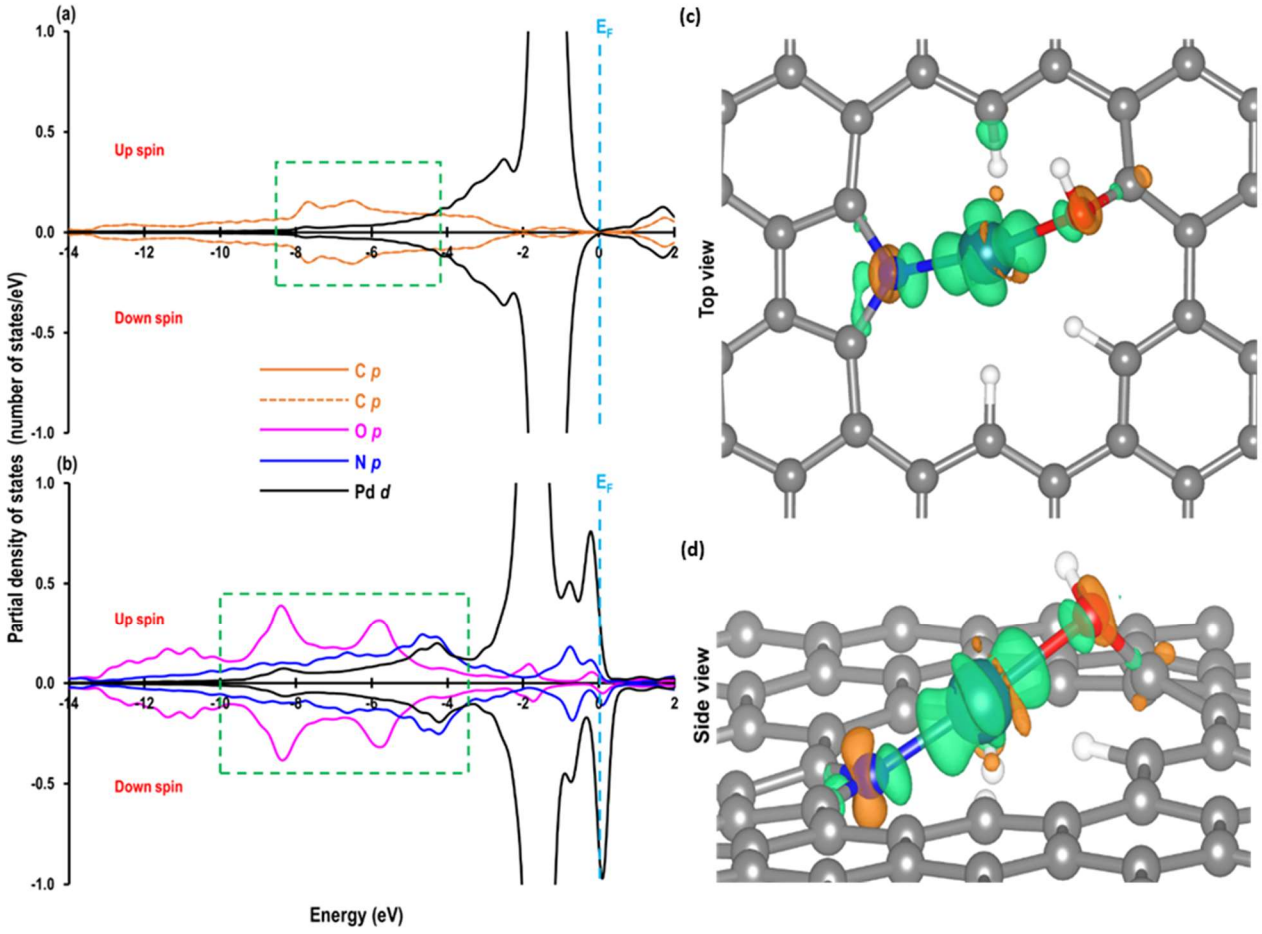

Fig. 8 The partial density of states (PDOS) of Pd (a) on G and (b) on the $N_{Pyr\text{-}OH}$. The relaxed structure of Pd adsorbed on graphene shows that Pd is bonded to two carbon atoms therefore for clarity the signatures of the two carbon atoms are indicated as solid and dotted lines. (c) Top-view and (d) side-view of the electron charge density difference (0.008 e/Å^3) of the adsorption of Pd-adatom on the $N_{Pyr\text{-}OH}$. Green lope represents electron depletion while brown lobes represents electron gain.

Table 1: The average particle-size, ECSA, $E_{1/2}$, mass and specific activities of the important samples used in the study.

Samples	Average Size (nm)	ECSA (m^2/g)	$E_{1/2}$ (V)	Mass activity at 0.9 V (A/mg)	Specific activity at 0.9 V (mA/cm^2)
Pd/NRGO-22%	9.0 ± 4.0	13.4	0.85	0.07	0.5
Pd/NRGO- *in-situ* (32% loading)	4.0 ± 2.0	15.0	0.93	0.59	3.96
Pd/NRGO-47%	5.0 ± 3.0	14.7	0.88	0.15	1.0
Pd/NRGO *ex-situ* (32% loading)	4.5 ± 2.0	13.1	0.90	0.25	1.94
Pd/RGO	6.0 ± 2.0	-	0.86	0.13	-
Pt/C	-	11.7	0.86	0.12	0.97